



Research Article

Room-temperature in situ synthesis of BiOBr/Bi₂O₃ composites for the catalytic degradation of ciprofloxacin using indoor fluorescent light illumination

Saifullahi Shehu Imam¹ · Rohana Adnan¹  · Noor Haida Mohd Kaus¹

© Springer Nature Switzerland AG 2019

Abstract

In this study, a complete room-temperature process for the synthesis of BiOBr/Bi₂O₃ composites has been developed. The process is facile, rapid and gives high yield. Initially, BiOBr photocatalyst was synthesized via solid-state synthesis using polyethylene glycol 400 (PEG400) as a morphology control agent. Subsequently, an in situ method in aqueous NaOH solution was adopted for the conversion of pristine BiOBr to BiOBr/Bi₂O₃ composites with variable proportion of α-Bi₂O₃, at room-temperature. Alkali etching duration played a key role towards crystalline, surface, morphological and optical properties of BiOBr/Bi₂O₃ composites, as confirmed by XRD, SEM, XPS, FTIR, UV-DRS, BET and PL characterizations. Compared to pristine BiOBr, the BiOBr/Bi₂O₃ composites exhibited high activity for ciprofloxacin (CIP) degradation under indoor fluorescent light illumination. Their photocatalytic activity increases with the increase in etching duration up to a period of 60 min and then decreases. The degradation efficiency of aqueous CIP solution (100 mL, 20 ppm) reached 95.3% within 90 min in the presence of BiOBr/Bi₂O₃-60 which showed the best performance, and the composite remained stable even after five consecutive cycles. Meanwhile, photogenerated holes (h⁺) and superoxide radical anions (·O₂⁻) were found to be the dominant degrading species during active species studies, and a possible mechanism for the photocatalytic degradation of CIP over BiOBr/Bi₂O₃-60 composite photocatalyst has been proposed.

Keywords BiOBr · BiOBr/Bi₂O₃ · Ciprofloxacin · Photocatalytic degradation · Indoor fluorescent light

1 Introduction

Due to their frequent use in human and veterinary medicine, current worldwide consumption of fluoroquinolones is about 44 million kilograms annually [1]. Among the fluoroquinolones, ciprofloxacin, CIP (Table 1) is commonly used as a first choice medication for curing complicated skin and urinary tract infections [2]. However after ingestion, CIP is only partially metabolized in the body, and high percentage of the antibiotic is being excreted into the environment, which subsequently remains stable due to its low degradability [3]. The presence of CIP in the environment has been reported to inhibit spinach plants growth [4]. Furthermore, new bacterial species that with

time spread antibiotic resistant genes also emerge [5]. As identified by the World Health Organization (WHO), such dissemination of antibiotic resistant genes is a great threat to human health and survival [6]. Thus, the eradication of antibiotics from the environment is very necessary.

A very famous technique for the removal of organic pollutants including antibiotics from the environment is heterogeneous photocatalysis, using TiO₂ [7]. Visible light is abundant and represents about 46% of the energy from the sun. Unfortunately, due to its wide band gap value of 3.2 eV, only UV light activates TiO₂. In view of the limited portion of UV light from the sun, demand for visible light active photocatalysts is now an issue on the rise. However, even with the provision of

✉ Rohana Adnan, r_adnan@usm.my | ¹School of Chemical Sciences, Universiti Sains Malaysia, 11800 Penang, Malaysia.

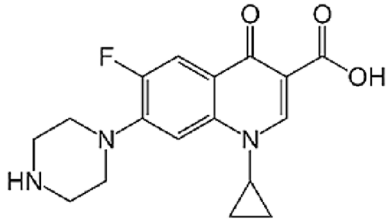


SN Applied Sciences (2019) 1:845 | <https://doi.org/10.1007/s42452-019-0851-3>

Received: 18 March 2019 / Accepted: 27 June 2019 / Published online: 10 July 2019

SN Applied Sciences
A SPRINGER NATURE journal

Table 1 Molecular structure some physicochemical properties of CIP

| Property | CIP |
|---|---|
| Chemical formula | C ₁₇ H ₁₈ FN ₃ O ₃ |
| Therapeutic group | Antibiotic |
| Chemical structure |  |
| Molecular weight (g mol ⁻¹) | 331.3 |
| Isoelectric constants | pK _{a1} =6.1; pK _{a2} =8.7 |

visible-light active photocatalysts, sometimes weather challenges such as during haze and rainy days, becomes another limitation. Sequel to that, the indoor application of photocatalysis is now a propitious alternative. Our preference for indoor fluorescent light illumination in this research is obviously because of its safety, efficiency and elongated lifetime [8].

Among the famous alternatives to TiO₂, Bi-based semiconductors including Bi₂O₃ [9], Bi₂S₃ [10], Bi₂WO₆ [11] and BiOX (X = Cl, Br and I) [12], are continuously gaining more attention on account of their prospective application in catalysis. Within the bismuth oxyhalides, BiOBr is a simple p-type semiconductor having a band gap of about 2.61–2.90 eV [13, 14]. It consists of tetragonal [Bi₂O₂]²⁺ slabs doubly interleaved by slabs of Br⁻ atoms to form [Bi₂O₂Br₂] layers [15]. Although it responds to visible light, however, BiOBr absorbs only a fraction. This in addition to the recombination of photoinduced electron–hole pairs, makes the visible light activity of BiOBr limited. Fortunately, the performance of BiOBr could be improved by forming heterojunctions in the form of BiOBr/FeWO₄ [16], BiOBr/Bi₂O₂CO₃ [17], BiOBr/NaBiO₃ [18] and BiOBr/BiPO₄ [19]. Such heterojunction might result in enhanced visible light absorption and/or prevent charge carriers' recombination.

In this study, both pristine BiOBr and BiOBr/Bi₂O₃ composites were synthesized through a facile and stepwise room-temperature production process, that combines both technical and economic feasibility. Subsequently, the catalysts were characterized using various techniques, and their photocatalytic performance was assessed by degrading aqueous CIP solution (100 mL, 20 ppm), under indoor fluorescent light illumination.

2 Experimental

2.1 Materials

Ciprofloxacin (C₁₇H₁₈FN₃O₃) was purchased from Sigma-Aldrich. Polyethylene glycol 400 (PEG 400) was obtained from Merck Chemicals. Bismuth nitrate pentahydrate (Bi(NO₃)₃·5H₂O), ascorbic acid (C₆H₈O₆), ethanol (CH₃CH₂OH), sodium hydroxide (NaOH) and isopropanol (C₃H₈O) were provided by QReC Chemicals. Potassium bromide salt (KBr) was obtained from HMBG Chemicals. Disodium ethylenediaminetetraacetic acid salt (EDTA-2Na) was obtained from R&M Chemicals. All received reagents were used without further purification.

2.2 Synthesis of pristine BiOBr and BiOBr/Bi₂O₃ composites

The homogeneity of the reaction mixture was considered important during the synthesis of BiOBr/Bi₂O₃ composites. Consequently, 5 mmol of Bi(NO₃)₃·5H₂O was initially grinded in an agate mortar for 10 min. After which, 3 mL of morphology control agent PEG 400 was added, and the mixture was further homogenized for 5 min. Finally, 5 mmol of KBr was added and likewise followed by 20 min grinding, producing an end product. The mixture was washed using DI water and absolute ethanol, and then dried at 60 °C for 10 h. The dried product was identified to be pristine BiOBr and was subsequently used as the template for the synthesis of BiOBr/Bi₂O₃ composites. To achieve this, 1 g of the pristine BiOBr was treated in 200 mL of 0.2 M NaOH and stirred at different time i.e. 10, 30, 60 and 120 min, at room-temperature. The composites were collected and again purified by washing with DI H₂O and absolute ethanol, and then dried at 60 °C for 10 h. The samples were labeled as BiOBr/Bi₂O₃-10, BiOBr/Bi₂O₃-30, BiOBr/Bi₂O₃-60 and BiOBr/Bi₂O₃-120 based on the alkali etching duration.

2.3 Characterizations

Phase composition of as-synthesized samples were characterized using advanced X-ray diffractometer (BRUKER AXS D8) with Cu-Kα X-rays source and sodium iodide scintillator type detector. Data was collected in the 2θ range of 10° < θ < 70°. Field emission scanning electron microscopy (Leo Supra 50 VP) was used to investigate the morphology of the samples. Shimadzu XPS Axis Ultra DLD instrument was used in conducting surface composition analysis, and the results were further deconvoluted using CASA XPS software. Micromeritics (ASAP 2020 V4.01)

instrument was used to obtain the isotherms for nitrogen adsorption–desorption. Photoluminescence (PL) spectra were recorded at room temperature using a Shimadzu RF-5300PC spectrofluorophotometer. Attenuated total reflectance Fourier transform-infrared (ATR-FTIR) spectra of the samples were recorded using FT-NIR spectroscopy (Perkin Elmer Spotlight 2000). UV–vis diffused reflectance spectra (DRS) of samples were recorded on a spectrophotometer (Cary 5000).

2.4 Photocatalytic activity test

The photocatalytic activities of pristine BiOBr and BiOBr/Bi₂O₃ composites were determined by degrading aqueous CIP solution using indoor fluorescent light (Panasonic FL40SS.D/36, 36 Watts) as the illumination source. The procedure involves dispersing 100 mg of the photocatalyst in a 250 mL Pyrex beaker containing 100 mL of 20 ppm aqueous CIP solution. The suspension was initially maintained in the dark for 30 min with stirring, to attain good dispersion and to establish adsorption–desorption equilibrium. It was subsequently illuminated with indoor fluorescent light under continuous stirring. At a constant time interval, 5 mL aliquots of reaction suspension were withdrawn using a syringe and the photocatalyst particles were removed via centrifugation at 4000 rpm for 10 min. Subsequently, the supernatant was quickly analyzed for the remnant CIP concentration using Shimadzu 2600, UV–Vis spectrophotometer version 1.03 equipped with UV Probe 2.42 software. The maximum absorbance at 276 nm was adopted for the measurement of temporal change in CIP concentration using deionized water as a reference sample. During mineralization studies, total organic carbon content was analyzed using Shimadzu TOC-L analyzer.

2.5 Degradation kinetics

Pseudo-first-order (Eq. 1) and pseudo-second-order (Eq. 2) are widely used models in describing the kinetics for the photocatalytic oxidation of many organic compounds [20]. In this study, the kinetics for the photocatalytic degradation of CIP using pristine BiOBr and BiOBr/Bi₂O₃ composites was determined by fitting the experimental degradation data to pseudo-first-order and pseudo-second-order models, as expressed below:

$$\ln\left(\frac{C_0}{C_t}\right) = k_1 t \quad (1)$$

$$\frac{1}{C_t} = \frac{1}{C_0} + k_2 t \quad (2)$$

where C_0 and C_t are the CIP concentration at irradiation time '0' and 't', k_1 is the pseudo-first-order rate constant and k_2 is the pseudo-second-order rate constant. The validity of the rate constant is determined by the correlation coefficient (R^2) value of the kinetic plot [21].

2.6 Active species studies

Active species trapping experiment was conducted using similar experimental procedure described in Sect. 2.4, except adding 1 mmol L⁻¹ disodium ethylenediaminetetraacetic acid salt (EDTA-2Na), 1 mmol L⁻¹ ascorbic acid (AA) and 10 mmol L⁻¹ isopropyl alcohol (IPA) in order to scavenge holes (h^+), superoxide radicals (O_2^-) and hydroxyl radicals ($\cdot OH$).

2.7 Photocatalyst recyclability

A total of 5 consecutive experiments were repeated to test the stability of the spent photocatalyst for the repeated degradation of aqueous ciprofloxacin solution, under indoor fluorescent light illumination. For this purpose, after every cycle, the spent photocatalyst was washed twice using deionized water, rinsed with absolute ethanol and then dried at 60 °C for 10 h, before subsequent use.

3 Results and discussion

3.1 XRD analysis

XRD patterns of pristine BiOBr and BiOBr/Bi₂O₃ composites with different Bi₂O₃ contents are shown in Fig. 1. In the case of pristine BiOBr, (001), (002), (101), (102), (110), (111), (112), (200), (113), (201), (104), (211), (114), (212), (204) and (220) diffraction peaks at 2θ values of 10.9°, 21.9°, 25.1°, 31.7°, 32.2°, 34.0°, 39.3°, 46.2°, 46.8°, 47.3°, 50.6°, 53.4°, 56.2°, 57.1°, 66.2° and 67.4° are well indexed to the standard data for the tetragonal phase of BiOBr [22]. The absence of stray peaks indicates the high purity of as-synthesized pristine BiOBr. Figure 1b is the enlarged XRD pattern in the range of $2\theta = 20^\circ - 35^\circ$, so as to further verify the transformation process from pristine BiOBr to BiOBr/Bi₂O₃ composites. Firstly, the impact of alkali etching duration on the spectrum of pristine BiOBr could be explained using the (111), (120), (012) and (200) diffraction peaks belonging to α -Bi₂O₃ (JCPDS No. 41-1449) [23]. From the figure, it is clear that, 10 min of alkali etching has minor influence on the spectrum of pristine BiOBr, since no diffraction peaks of α -Bi₂O₃ were sighted, but only a slight decrease in the intensity of pristine BiOBr diffraction peaks. As etching duration reaches 30 min, the emergence of (120) diffraction peak belonging to α -Bi₂O₃ could

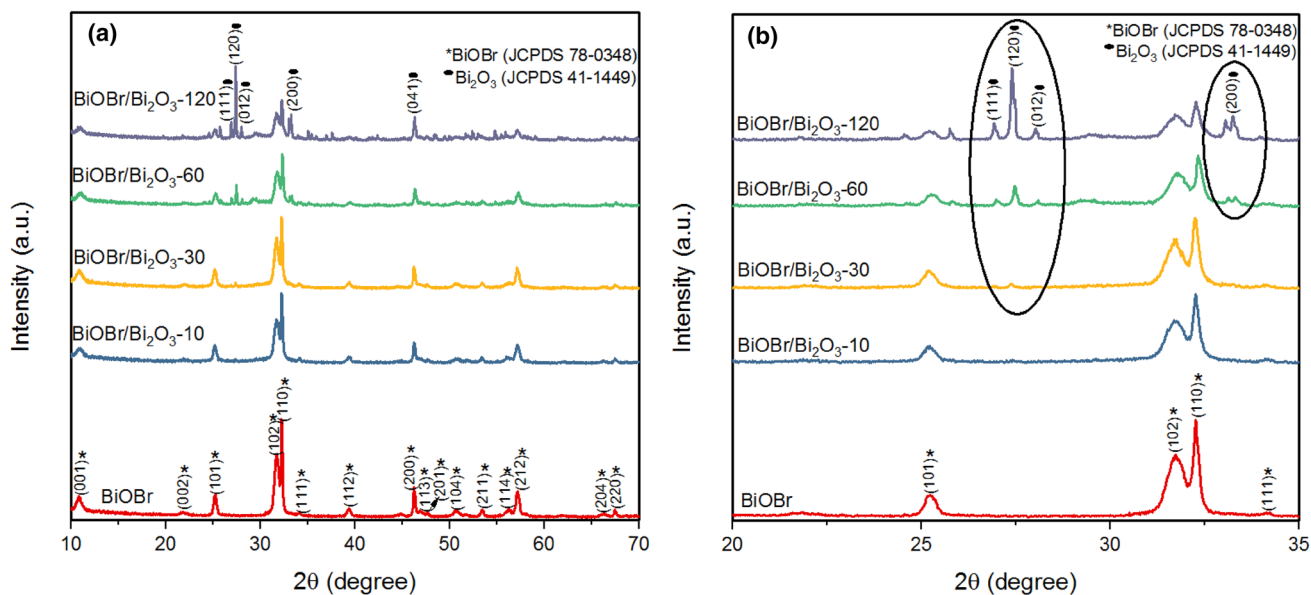


Fig. 1 XRD pattern of as-synthesized **a** pristine BiOBr and BiOBr/Bi₂O₃ composites, **b** enlarged view of diffraction region between 20° and 35°

Table 2 Crystalline size and micro-strain of pristine BiOBr and BiOBr/Bi₂O₃ composites photocatalysts

| Sample | FWHM | Crystalline size (nm) | Micro-strain |
|---|--------|-----------------------|--------------|
| BiOBr | 0.0984 | 87 | 0.0015 |
| BiOBr/Bi ₂ O ₃ -10 | 0.1378 | 62 | 0.0021 |
| BiOBr/Bi ₂ O ₃ -30 | 0.1378 | 62 | 0.0021 |
| BiOBr/Bi ₂ O ₃ -60 | 0.1181 | 73 | 0.0018 |
| BiOBr/Bi ₂ O ₃ -120 | 0.1378 | 62 | 0.0025 |

be observed. After 60 min of alkali etching, (111), (120), (012) and (200) diffraction peaks of α-Bi₂O₃ becomes readily visible, although with low intensity, while 120 min of alkali etching makes the appearance of α-Bi₂O₃ diffraction peaks to become more intense. However, from the figure, it is clear that, despite the 120 min alkali etching duration, complete conversion of BiOBr to absolute α-Bi₂O₃ was not achieved, as diffraction peaks such as (101), (102) and (110) belonging to tetragonal phase of BiOBr are still present, although with low intensity. This signifies the co-existence of BiOBr and α-Bi₂O₃ in BiOBr/Bi₂O₃ composites.

Furthermore, the crystalline size (*d*) and micro-strain (ϵ) values of pristine BiOBr and BiOBr/Bi₂O₃ composites are calculated using Eqs. (3) and (4), and the results are summarized in Table 2.

$$d = \frac{0.9\lambda}{\beta \cos\theta} \tag{3}$$

$$\epsilon = \frac{\beta}{4\tan\theta} \tag{4}$$

where λ is the wavelength of the XRD, β is the full width at half maximum (FWHM) of the diffraction peak and θ is the diffraction angle.

From Table 2, it is clear that BiOBr/Bi₂O₃ composites have average crystalline size around 62–75 nm, with BiOBr/Bi₂O₃-60 having the least micro-strain value, an indication of good crystalline nature of BiOBr/Bi₂O₃-60 composite [24].

3.2 FESEM analysis

FESEM analysis was carried out to determine the morphology of pristine BiOBr and the effect of alkali etching duration on the morphology of BiOBr/Bi₂O₃ composites. As shown in Fig. 2a, b, pristine BiOBr is composed of individual nanosheets with thickness in the range of 22–24 nm, which assembled to form a porous flower-like structure with an average diameter in the range of 1.8–2.1 μm. With the commencement of alkali etching treatment, a change in morphology of the etched BiOBr samples was observed and varies based on the etching duration. For instance, 10 min of alkali etching treatment leads to a slight crumbling in the porous flower-like morphology. After 30 min of etching treatment, early stage growth of α-Bi₂O₃ rods was sighted. After 60 min etching treatment, α-Bi₂O₃ rods surrounded by BiOBr have been formed, with an average diameter in the range of 650–750 nm. However, as shown in Fig. 2f, after 120 min of alkali etching treatment, α-Bi₂O₃

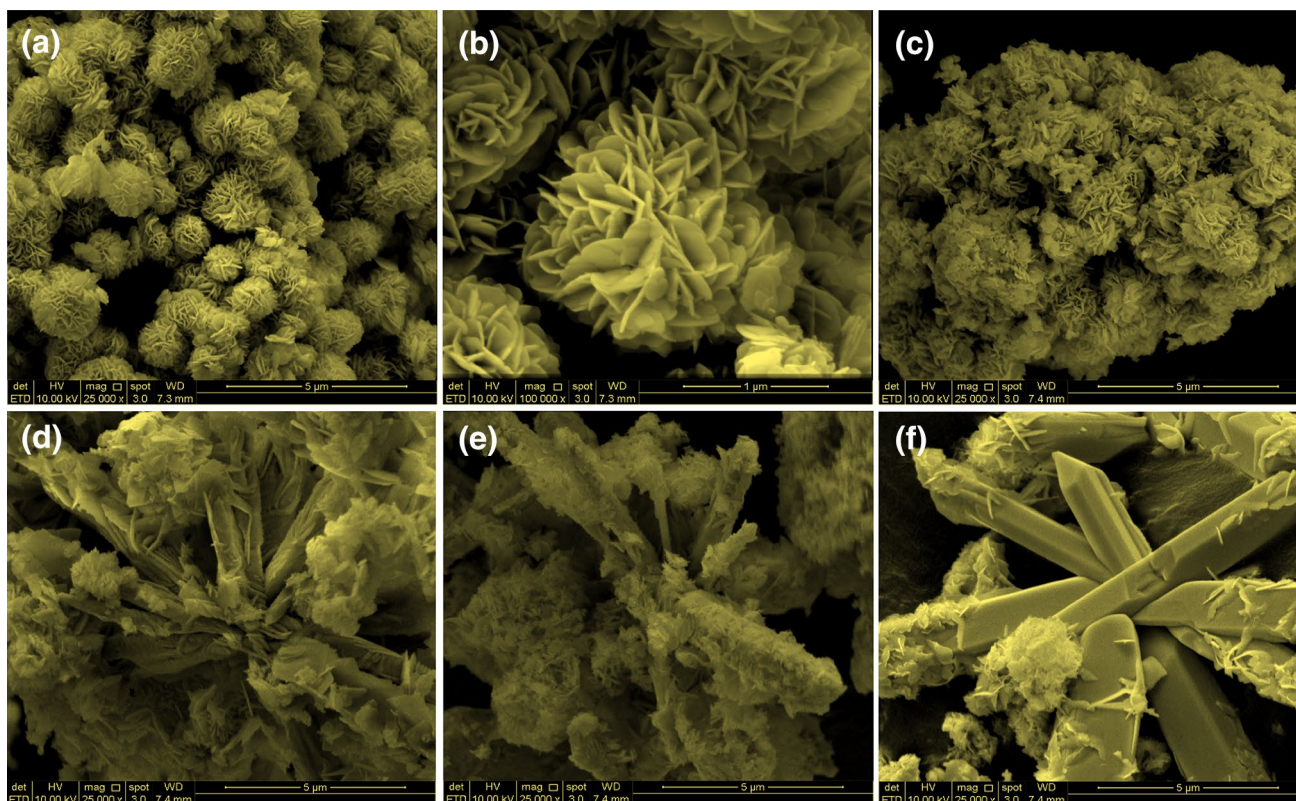


Fig. 2 FESEM images of pristine BiOBr (**a, b**), BiOBr/Bi₂O₃-10 (**c**), BiOBr/Bi₂O₃-30 (**d**), BiOBr/Bi₂O₃-60 (**e**) and BiOBr/Bi₂O₃-120 (**f**)

rods formed giant rod-like structures having an average diameter in the range of 1–2.5 μm, and very less BiOBr nanosheets around the rods. In summary, NaOH played the role of being a dehalogenation agent. Therefore, the transformation from pristine BiOBr to BiOBr/Bi₂O₃ composites happens because during the etching process, alkali cleavage results in the decay of Br atom in BiOBr. The Bi³⁺ ions are unstable in alkaline solution, and subsequently precipitate on the outer surface of BiOBr and transform into α-Bi₂O₃ phase. Sequel to that, extending alkali etching duration leads to more α-Bi₂O₃ phase.

3.3 FTIR-ATR analysis

The chemical structures of pristine BiOBr and BiOBr/Bi₂O₃ composites were further analyzed by examining surface functional groups of the photocatalysts using FTIR-ATR analysis in the range of 600–3800 cm⁻¹ and the spectra is shown in Fig. 3. For the pristine BiOBr, absorption bands in the range of 600–1000 cm⁻¹ are related to the stretching vibration of Bi–O bond [25], while those between 1000 and 1500 cm⁻¹ belongs to Bi–Br band [26]. In the case of BiOBr/Bi₂O₃ composites, obvious changes which have been attributed to the partial conversion of BiOBr into BiOBr/Bi₂O₃ composites were observed. For instance,

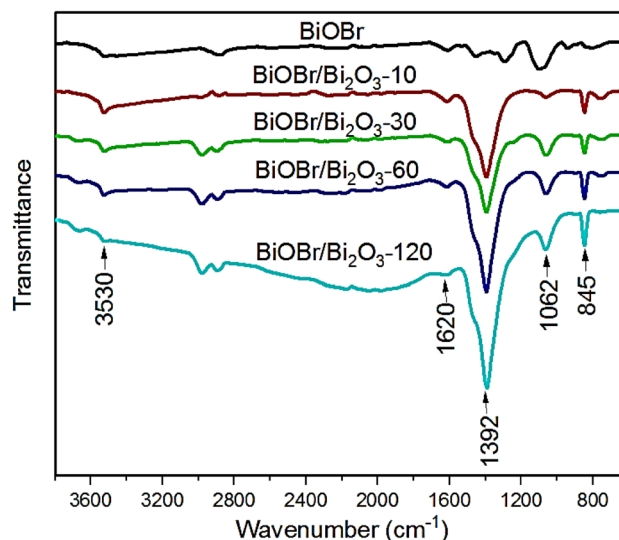


Fig. 3 FTIR spectra of as-synthesized pristine BiOBr and BiOBr/Bi₂O₃ composites

new band appears at about 1062 cm⁻¹, and its intensity increases with increase in alkali etching duration. Such band is attributed to the new vibrations resulting from interaction of Bi–O bonds in Bi₂O₃ with their surroundings

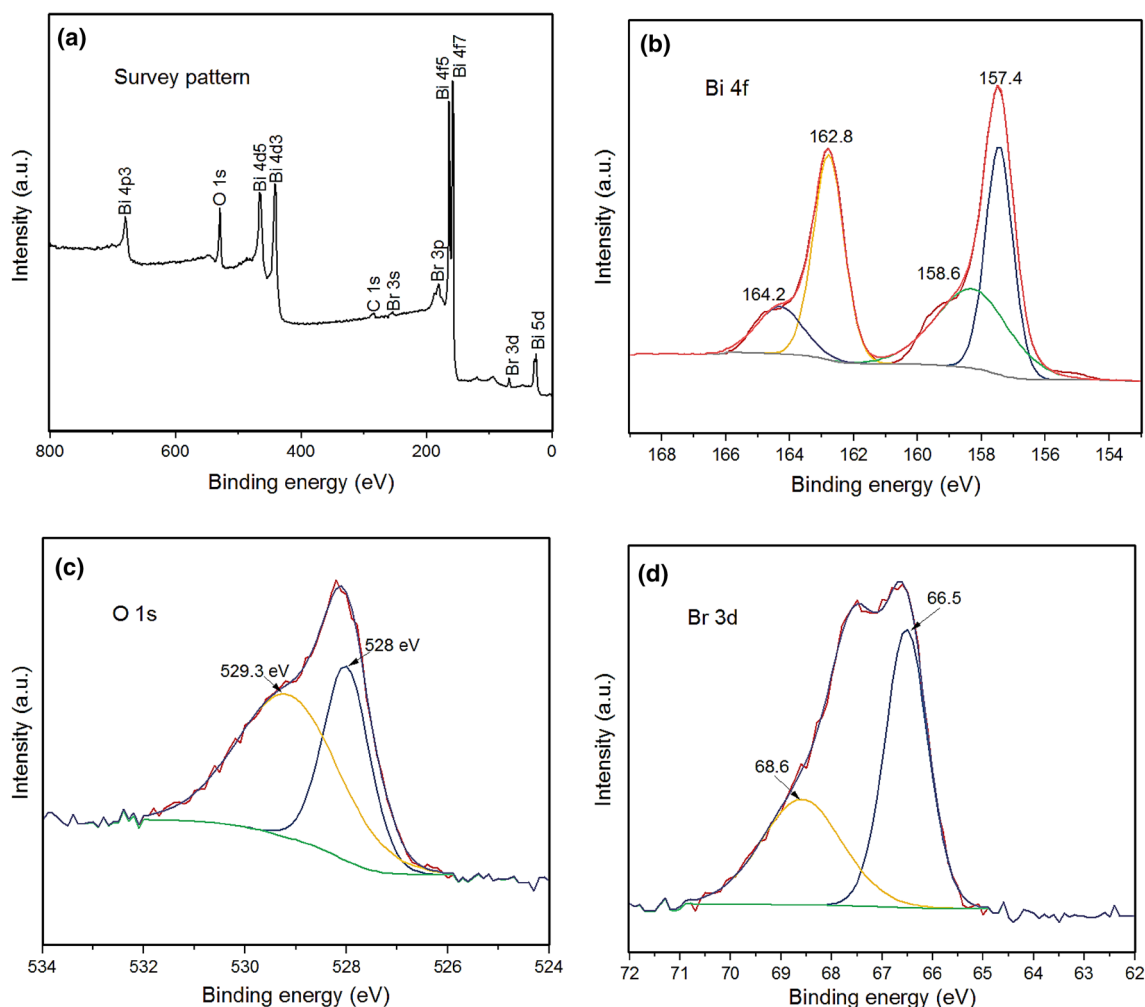


Fig. 4 XPS spectra of BiOBr/Bi₂O₃-60 composite: **a** survey spectrum, **b** Bi 4f, **c** O 1s and **d** Br 3d

[27]. Finally, carbon dioxide from the atmosphere, following etching treatment which is conducted in air, gave rise to the bands at about 845 and 1392 cm⁻¹ in the BiOBr/Bi₂O₃ composites. In general, for both pristine BiOBr and BiOBr/Bi₂O₃ composites, bands at about 1620 cm⁻¹ and 3530 cm⁻¹ are due to bending vibrations of free water molecules and O–H stretching vibrations [28].

3.4 XPS analysis

Surface composition and chemical state of BiOBr/Bi₂O₃-60 composite photocatalyst was further investigated using X-ray photoelectron spectroscopy. Figure 4 consists of a full survey pattern and high resolution Bi 4f, O 1s and Br 3d spectra of BiOBr/Bi₂O₃-60 composite. Survey spectrum in Fig. 4a confirms the existence of Bi, O and Br elements on the surface of BiOBr/Bi₂O₃-60 composite. The Bi 4f spectrum in Fig. 4b shows a binding energy at 157.4 eV for Bi 4f_{7/2} and at 162.8 eV for Bi 4f_{5/2}, of Bi³⁺ in BiOBr [29].

Subsequent deconvolution of the Bi 4f spectrum leads to the formation of two new peaks at 158.6 eV and 164.2 eV, which are due to Bi³⁺ from Bi₂O₃ [30]. The O 1s spectrum can also be deconvoluted into two peaks at 528 eV and 529.3 eV, which are ascribed to Bi–O in BiOBr and Bi–O in Bi₂O₃ [31]. Finally, the slight shift to lower binding energy of the two peaks in the Br 3d spectrum at 66.6 eV and 68.7 eV ascribed to Br 3d_{5/2} and Br 3d_{3/2} further confirms the interface interaction between BiOBr and Bi₂O₃ [32].

3.5 Optical absorption property

Optical absorption property of pristine BiOBr and BiOBr/Bi₂O₃ composites was probed using UV–Vis diffuse reflectance spectroscopy. The digital images of pristine BiOBr and BiOBr/Bi₂O₃ composites are shown in Fig. 5a, where the color of the composites gradually deepens as etching duration is being extended. It is clear from Fig. 5b that, both pristine BiOBr and BiOBr/Bi₂O₃ composites

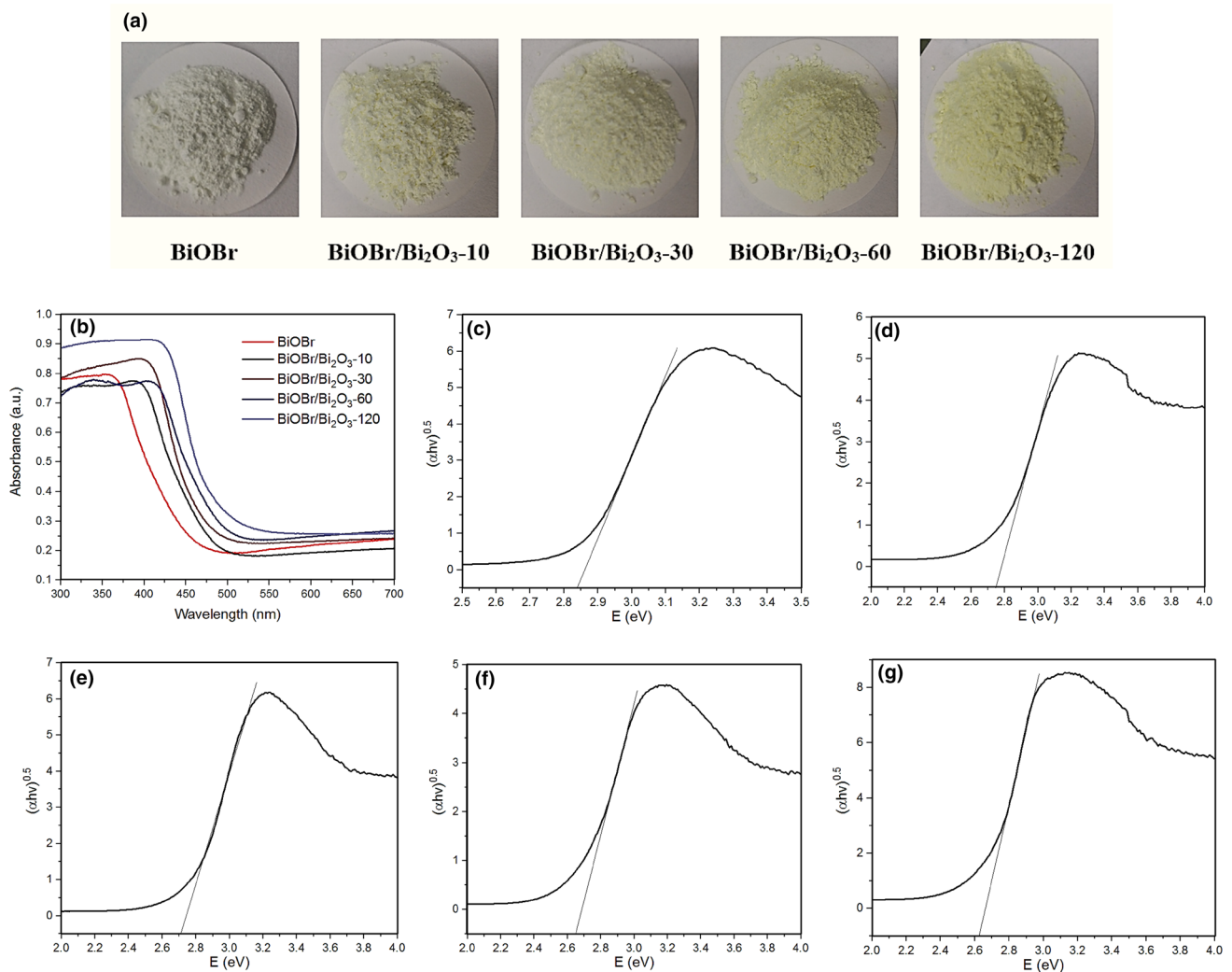


Fig. 5 Digital images of pristine BiOBr and BiOBr/Bi₂O₃ composites (a) UV-Vis diffuse reflectance spectra of pristine BiOBr and BiOBr/Bi₂O₃ composites (b) and Tauc's plot of $(\alpha h\nu)^{0.5}$ versus E (eV) for as-

synthesized pristine BiOBr (c), BiOBr/Bi₂O₃-10 (d), BiOBr/Bi₂O₃-30 (e), BiOBr/Bi₂O₃-60 (f) and BiOBr/Bi₂O₃-120 (g)

have absorption edges in the visible region, with the absorption edges of BiOBr/Bi₂O₃ composites shifting slightly to longer wavelengths as alkali-etching duration is being extended. Such result is an indication that, the formation of heterojunction between pristine BiOBr and α -Bi₂O₃ could result in more visible light photocatalytic activity. Subsequently, their band gap energy was evaluated using Tauc's equation based on DRS results.

$$\alpha h\nu = A(h\nu - E_g)^{n/2} \quad (5)$$

where α , u , A and E_g are the absorption coefficient, light frequency, proportionality constant and band gap energy. The intercept of the tangent lines to the plot of $(\alpha h\nu)^{1/2}$ versus photon energy ($h\nu$) in Fig. 5c–g gave an estimate of the band gap. α -Bi₂O₃ has a band gap of about 2.55 eV

[33]. The band gaps of pristine BiOBr and BiOBr/Bi₂O₃ composites are summarized in Table 3.

3.6 Specific surface area and pore structure

Surface areas and pore size distribution of pristine BiOBr and BiOBr/Bi₂O₃ composites were determined by nitrogen adsorption and desorption isotherms, as shown in Fig. 6. From the figure, both pristine BiOBr and BiOBr/Bi₂O₃ composites have type IV sorption isotherm with H3 hysteresis loop, a common feature of catalysts with aggregation of nanosheets [34]. Pore size distribution (PSD) of the photocatalysts (as shown in the insets), range between 2 to more than 50 nm, thus indicating the co-existence of mesopores and

Table 3 Surface areas, pore parameters and band gap values of pristine BiOBr and BiOBr/Bi₂O₃ composite photocatalysts

| Samples | BET surface area (m ² /g) | Total pore volume (cm ³ /g) | Average pore diameter (nm) | Band gap (eV) |
|---|--------------------------------------|--|----------------------------|---------------|
| BiOBr | 17.09 | 0.095 | 24.40 | 2.84 |
| BiOBr/Bi ₂ O ₃ -10 | 16.83 | 0.060 | 16.33 | 2.75 |
| BiOBr/Bi ₂ O ₃ -30 | 15.86 | 0.058 | 15.24 | 2.71 |
| BiOBr/Bi ₂ O ₃ -60 | 15.26 | 0.057 | 14.58 | 2.65 |
| BiOBr/Bi ₂ O ₃ -120 | 10.82 | 0.036 | 13.45 | 2.62 |

macropores. The specific surface area was calculated using Brunauer–Emmet–Teller (BET) equation and the results are presented in Table 3. From the results, initially pristine BiOBr have a BET specific surface area of 17.0858 m² g⁻¹. Alkali etching for a period of 60 min gave a BiOBr/Bi₂O₃ composite with a BET specific surface area quite close to that of pristine BiOBr. However, extending alkali etching duration to a period of 120 min results in a significant decrease in BET specific surface area of BiOBr/Bi₂O₃-120 to 10.8216 m² g⁻¹. In summary, such a decrease in surface area of the BiOBr/Bi₂O₃ has been attributed to the conversion of pristine BiOBr from plates-like morphology to a mixture of plates-like and rod-like BiOBr/Bi₂O₃ composites. The decrease in pore size and volume is also attributed to the collapse of pores during the etching process.

3.7 Photoluminescence spectra

Figure 7 is the photoluminescence emission spectra of pristine BiOBr and various BiOBr/Bi₂O₃ composite photocatalysts. The recombination rate is predicted using the intensity of the photoluminescence, as lower photoluminescence intensity implies low recombination rate of photogenerated charge carriers, while higher photoluminescence intensity implies high recombination rate of photogenerated charge carriers [35]. Compared to pristine BiOBr, BiOBr/Bi₂O₃ composites have lower photoluminescence intensity, with the BiOBr/Bi₂O₃-60 composite having the least. Based on the results, the heterostructure formed between BiOBr and Bi₂O₃ could enhance the separation efficiency of photogenerated charge carriers.

3.8 Photocatalytic activity

Initially, a blank study conducted at ambient temperature and atmospheric pressure showed that CIP is not self-degradable under indoor fluorescent light illumination. Subsequently, the photocatalytic activity of the as-synthesized catalysts was evaluated by degrading CIP under the same condition. The UV spectra representing temporal change in aqueous solution of CIP is shown in Fig. 8a–e. The effective decomposition of CIP is represented by the

decrease in peak intensity at 276 nm. Figure 9a shows the photodegradation efficiency of CIP as a function of irradiation time using various photocatalysts. Due to the formed heterojunction, BiOBr/Bi₂O₃ composites displayed better photocatalytic activity as compared to pristine BiOBr which has low visible light catalytic activity. The degradation efficiency of CIP over pristine BiOBr is only 72.8% in 90 min, while 95.3% of CIP was photodegraded over BiOBr/Bi₂O₃-60 composite, which showed the best performance. The decrease in photodegradation efficiency in the case of BiOBr/Bi₂O₃-120 composite is related to the recombination of photogenerated charge carriers and possibly, the drastic loss in surface area.

Meanwhile, as shown in Fig. 10, the TOC value of 20 ppm ciprofloxacin solution was found to be 18.09 mg L⁻¹, but decreased to 11.29 mg L⁻¹, after 30 min adsorption by BiOBr/Bi₂O₃-60, and subsequently to 6.48 mg L⁻¹ after 90 min of photocatalytic degradation. Such results have further demonstrated the mineralization ability of BiOBr/Bi₂O₃-60 composite photocatalyst.

3.9 Degradation kinetics

The experimental data for the photocatalytic degradation of CIP using pristine BiOBr and BiOBr/Bi₂O₃ composite photocatalysts was subsequently examined using the pseudo-first-order and pseudo-second-order kinetic models. The value of the correlation coefficient (R²) of the kinetic plots was used in selecting the best fitted model.

3.9.1 Pseudo-first-order kinetic model

Figure 11 is the pseudo-first-order plot for the degradation of CIP by pristine BiOBr and BiOBr/Bi₂O₃ composite photocatalysts under indoor fluorescent light illumination. From the high value of the correlation coefficients, it could be predicted that, the degradation process follows pseudo-first-order kinetic model. Furthermore, from the rate constants presented in Table 4, the photocatalytic activity sequence is $k_{\text{BiOBr/Bi}_2\text{O}_3-60} > k_{\text{BiOBr/Bi}_2\text{O}_3-30} > k_{\text{BiOBr/Bi}_2\text{O}_3-10} > k_{\text{BiOBr/Bi}_2\text{O}_3-120} > k_{\text{BiOBr}}$ and

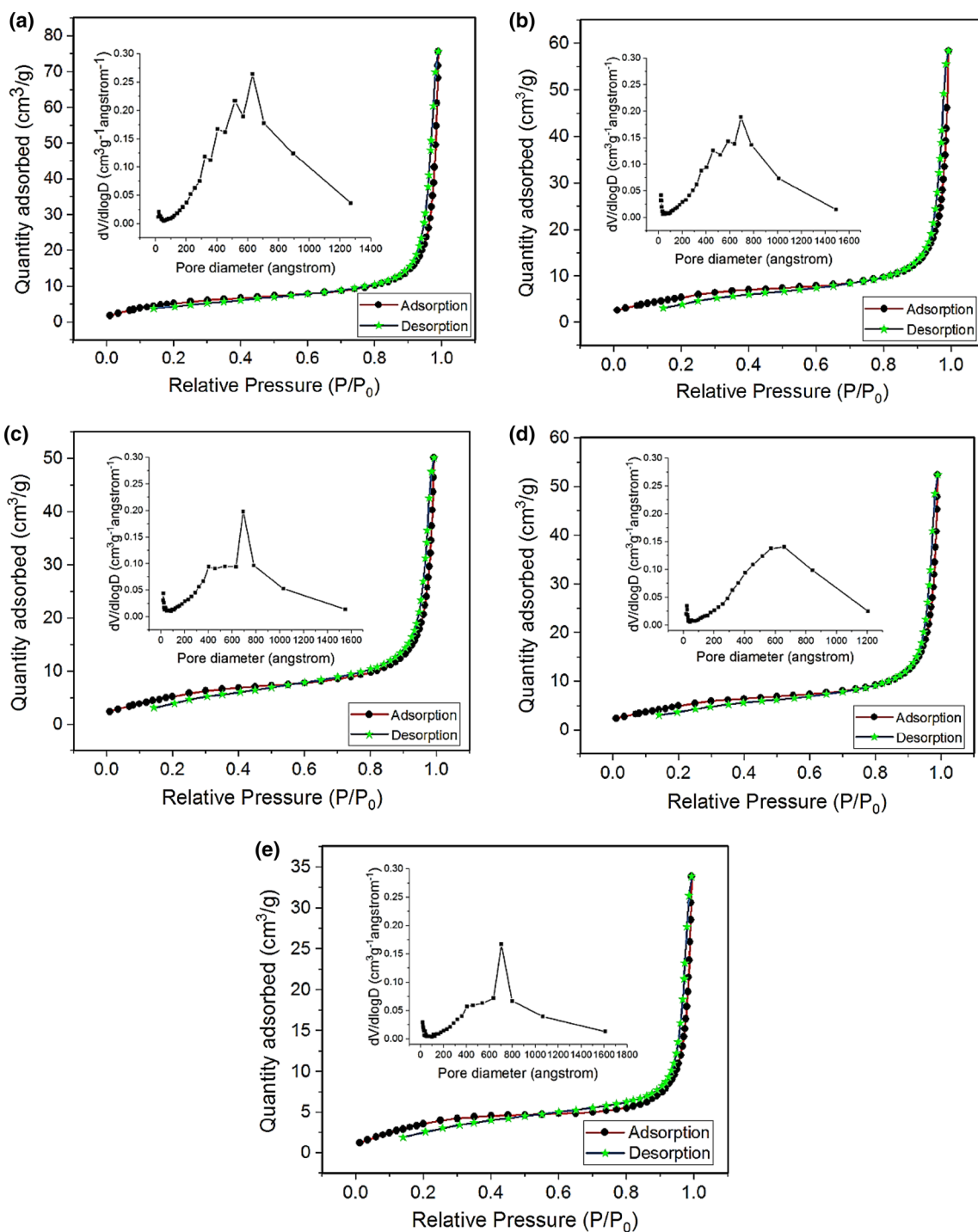


Fig. 6 N₂ adsorption–desorption isotherm of **a** pristine BiOBr, **b** BiOBr/Bi₂O₃-10, **c** BiOBr/Bi₂O₃-30, **d** BiOBr/Bi₂O₃-60 and **e** BiOBr/Bi₂O₃-120 composites. The inset is the corresponding pore size distribution

indication that optimized alkali etching duration has impact towards enhancing the visible-light performance of BiOBr.

3.9.2 Pseudo-second-order kinetic model

Figure 12 is the pseudo-second-order kinetic plot for the degradation of aqueous CIP solution using pristine BiOBr and BiOBr/Bi₂O₃ composite photocatalysts under indoor

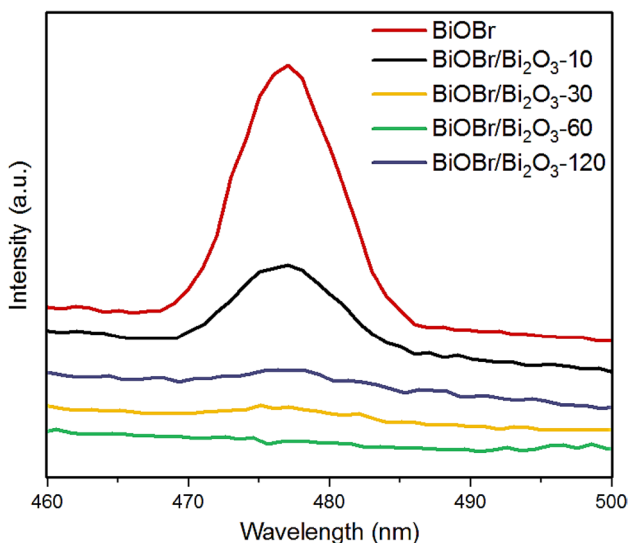


Fig. 7 Photoluminescence spectra of as-synthesized pristine BiOBr and BiOBr/Bi₂O₃ composites

fluorescent light illumination. As shown in Table 4, the pseudo-second-order kinetic model have low correlation coefficient (R^2) values compared to that of pseudo-first-order kinetic model. Such information can be used to conclude that, the degradation of aqueous CIP solution using

pristine BiOBr and BiOBr/Bi₂O₃ composite photocatalysts under indoor fluorescent light illumination does not fit the pseudo-second-order kinetic model.

As shown in Table 4, the pseudo-first-order rate constant for BiOBr/Bi₂O₃-60 is four times higher than that of pristine BiOBr. Such result has further demonstrated the enhanced visible light degradation of CIP by BiOBr/Bi₂O₃-60 composite.

3.10 Active species studies

This study was conducted by introducing various scavengers, with the purpose of quenching the activity of photogenerated species involved in the degradation of CIP by BiOBr/Bi₂O₃-60, and the results are presented in Fig. 13. From Fig. 13a, it is clear that, the degradation of CIP by BiOBr/Bi₂O₃-60 was significantly inhibited in the presence of EDTA-2Na and AA. This implies that holes (h^+) and superoxide radical anions ($\cdot O_2^-$) played a dominant role in the degradation of CIP by BiOBr/Bi₂O₃-60. However, the degradation of CIP by BiOBr/Bi₂O₃-60 remained uninhibited in the presence of IPA, an indication that hydroxyl radicals ($\cdot OH$) had no role in the photocatalytic degradation of CIP by BiOBr/Bi₂O₃-60. This can be confirmed from the rate constant (k) values in Table 5. Such findings revealed that,

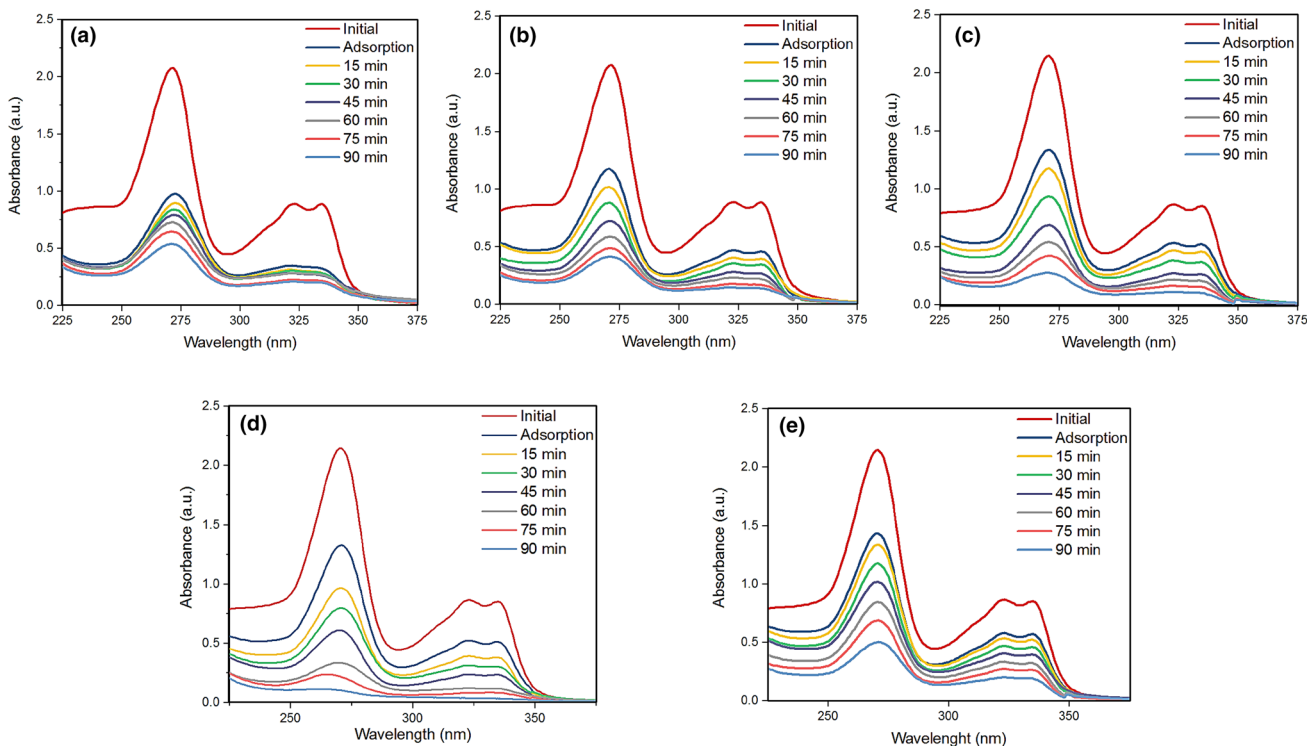


Fig. 8 Temporal evolution of the absorption spectrum of ciprofloxacin solution (20 ppm) in the presence of **a** pristine BiOBr, **b** BiOBr/Bi₂O₃-10, **c** BiOBr/Bi₂O₃-30, **d** BiOBr/Bi₂O₃-60 and **e** BiOBr/Bi₂O₃-120 composites under indoor fluorescent light illumination

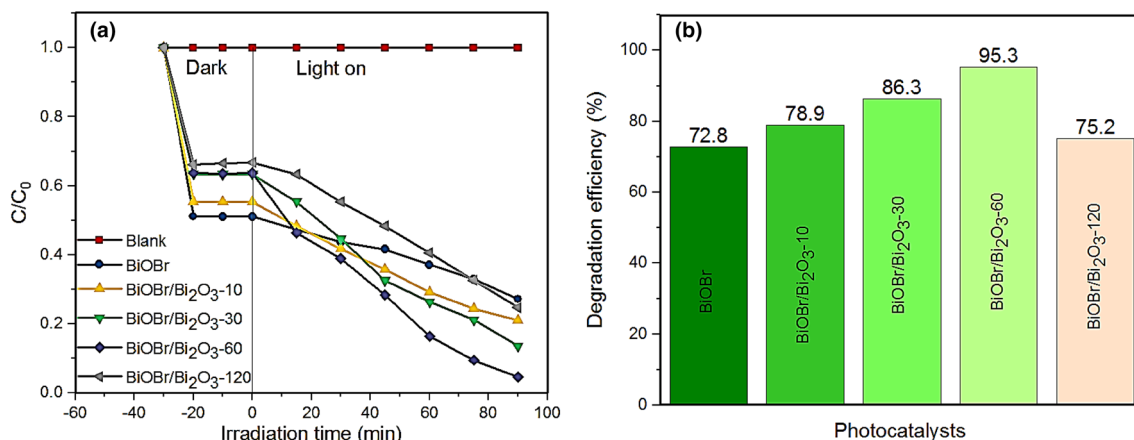


Fig. 9 Photocatalytic degradation curve (a) and efficiencies (b) of CIP degradation over pristine BiOBr and BiOBr/Bi₂O₃ composites under indoor fluorescent light illumination

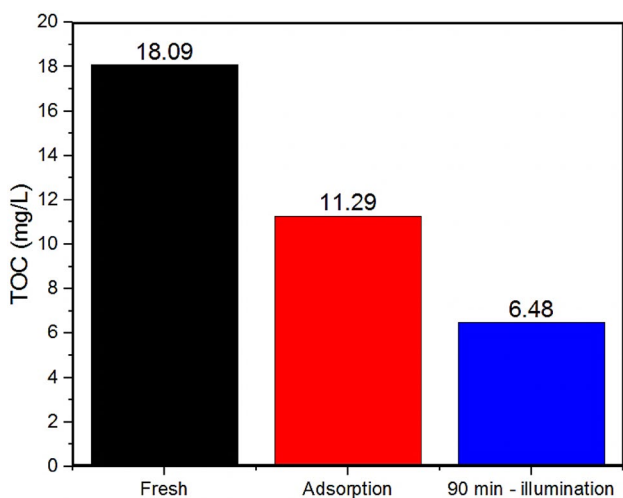


Fig. 10 TOC removal in the presence of BiOBr/Bi₂O₃-60 composite photocatalyst

holes (h⁺) and superoxide radical anions (·O₂⁻) are the main active species involved in the photocatalytic degradation of CIP by BiOBr/Bi₂O₃-60 composite.

3.11 Proposed photocatalytic mechanism

The mechanism for the photocatalytic degradation of CIP by BiOBr/Bi₂O₃-60 composite photocatalyst under indoor fluorescent light illumination would be proposed using results from active species studies which confirmed holes and superoxide radical anions as the main degrading species, photoluminescence which confirmed the separation of photogenerated charge carriers in BiOBr/Bi₂O₃-60 composite photocatalyst and by determining the valence band (VB) and conduction band (CB) edge potentials of

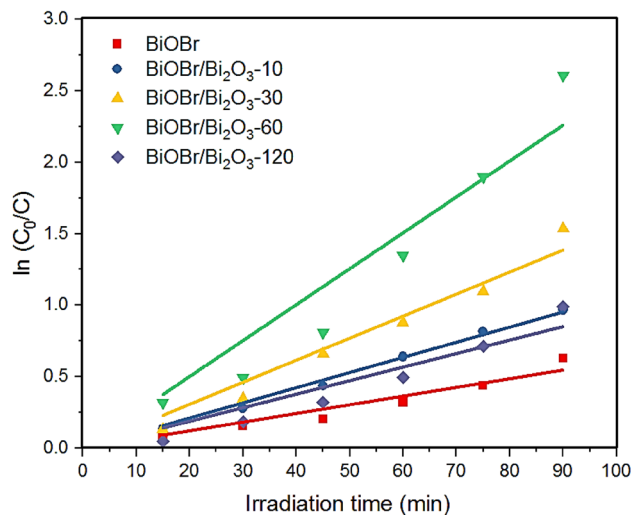


Fig. 11 Pseudo-first-order kinetic plot for the degradation of CIP using pristine BiOBr and BiOBr/Bi₂O₃ composite photocatalysts under indoor fluorescent light illumination

Table 4 Pseudo-first-order and pseudo-second-order rate constants and correlation coefficients for the photocatalytic degradation of CIP using pristine BiOBr and BiOBr/Bi₂O₃ composite photocatalysts

| Sample | Pseudo-first order rate model | | Pseudo-second order rate model | |
|---|-------------------------------|----------------|--------------------------------|----------------|
| | k (min ⁻¹) | R ² | k (min ⁻¹) | R ² |
| BiOBr | 0.00607 | 0.98122 | 8.043 × 10 ⁻⁴ | 0.95002 |
| BiOBr/Bi ₂ O ₃ -10 | 0.01058 | 0.99826 | 0.00156 | 0.97732 |
| BiOBr/Bi ₂ O ₃ -30 | 0.01540 | 0.98956 | 0.00264 | 0.90254 |
| BiOBr/Bi ₂ O ₃ -60 | 0.02511 | 0.97531 | 0.01038 | 0.70075 |
| BiOBr/Bi ₂ O ₃ -120 | 0.00945 | 0.97164 | 0.00113 | 0.91403 |

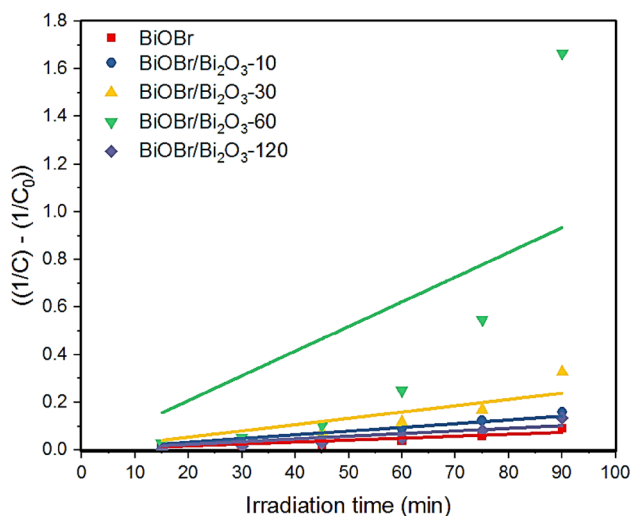


Fig. 12 Pseudo-second-order kinetic plot for the degradation of CIP using pristine BiOBr and BiOBr/Bi₂O₃ composite photocatalysts under indoor fluorescent light illumination

α -Bi₂O₃ and BiOBr and the schematic illustration is shown in Fig. 14.

BiOBr is a p-type semiconductor with bandgap of 2.84 eV having VB and CB at 3.096 and 0.256 eV, and a Fermi level close to its VB [36], while α -Bi₂O₃ is an n-type semiconductor with bandgap of 2.12 eV having VB and CB at 2.33 and 0.11 eV, and a Fermi level close to its CB [37]. Thus, when α -Bi₂O₃ and BiOBr are in contact, a p-n heterojunction will be formed upon successful equilibration of their Fermi levels. Such equilibration is possible via the downward movement of the Fermi level of α -Bi₂O₃,

Table 5 Correlation coefficients and rate constants of CIP degradation by BiOBr/Bi₂O₃-60 composite photocatalyst, in the absence and presence of various scavengers, under indoor fluorescent light illumination

| Radical quenchers | K (min ⁻¹) | R^2 |
|-------------------|--------------------------|--------|
| No scavenger | 0.02516 | 0.9751 |
| IPA | 0.02164 | 0.9886 |
| AA | 0.00375 | 0.9960 |
| EDTA-2Na | 0.00033 | 0.9616 |

and the upward movement of the Fermi level of BiOBr. It is important to further point out that, the positive movement of Fermi level of α -Bi₂O₃ promotes the positive shift of its VB and CB, while the negative movement by the Fermi level of BiOBr promotes the negative shift of its VB and CB [38].

Subsequently, upon illumination with visible light, both BiOBr and α -Bi₂O₃ will produce photogenerated charge carriers, however, since the CB edge of BiOBr is now at higher position due to the Fermi level upshift, and because of the breadth of the CB of BiOBr which permits the photoexcitation of electrons to high levels of CB [39], electrons at the CB of BiOBr yield $\cdot O_2^-$ by reacting with dissolved oxygen, while the direct oxidation ability of the BiOBr holes have decreased due to the rise in position of the VB of BiOBr. On the other hand, the electrons at the CB of α -Bi₂O₃ transfer and combine with the holes on the VB of BiOBr, a process that inhibits their recombination. Finally, the lowering in position of the holes of α -Bi₂O₃ due to Fermi level downshift strengthens their oxidation ability [40].

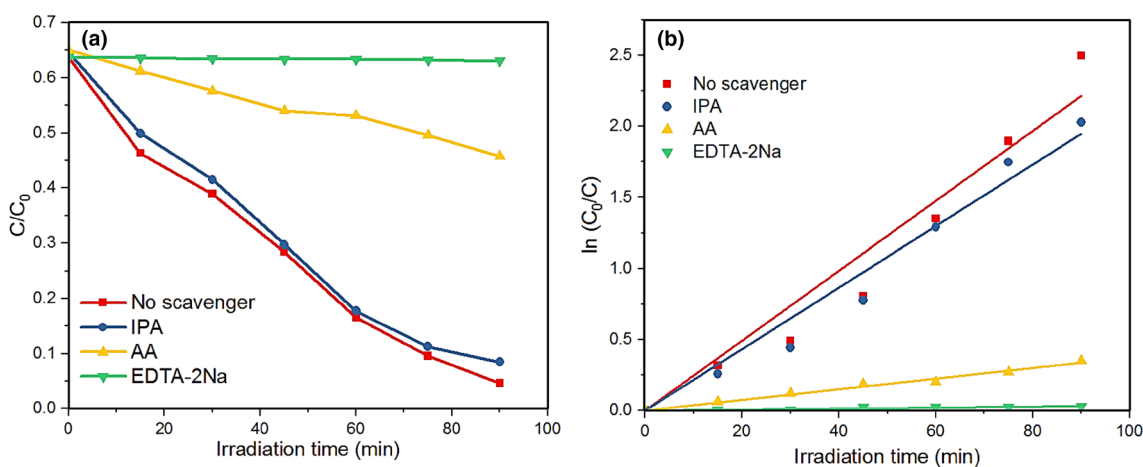
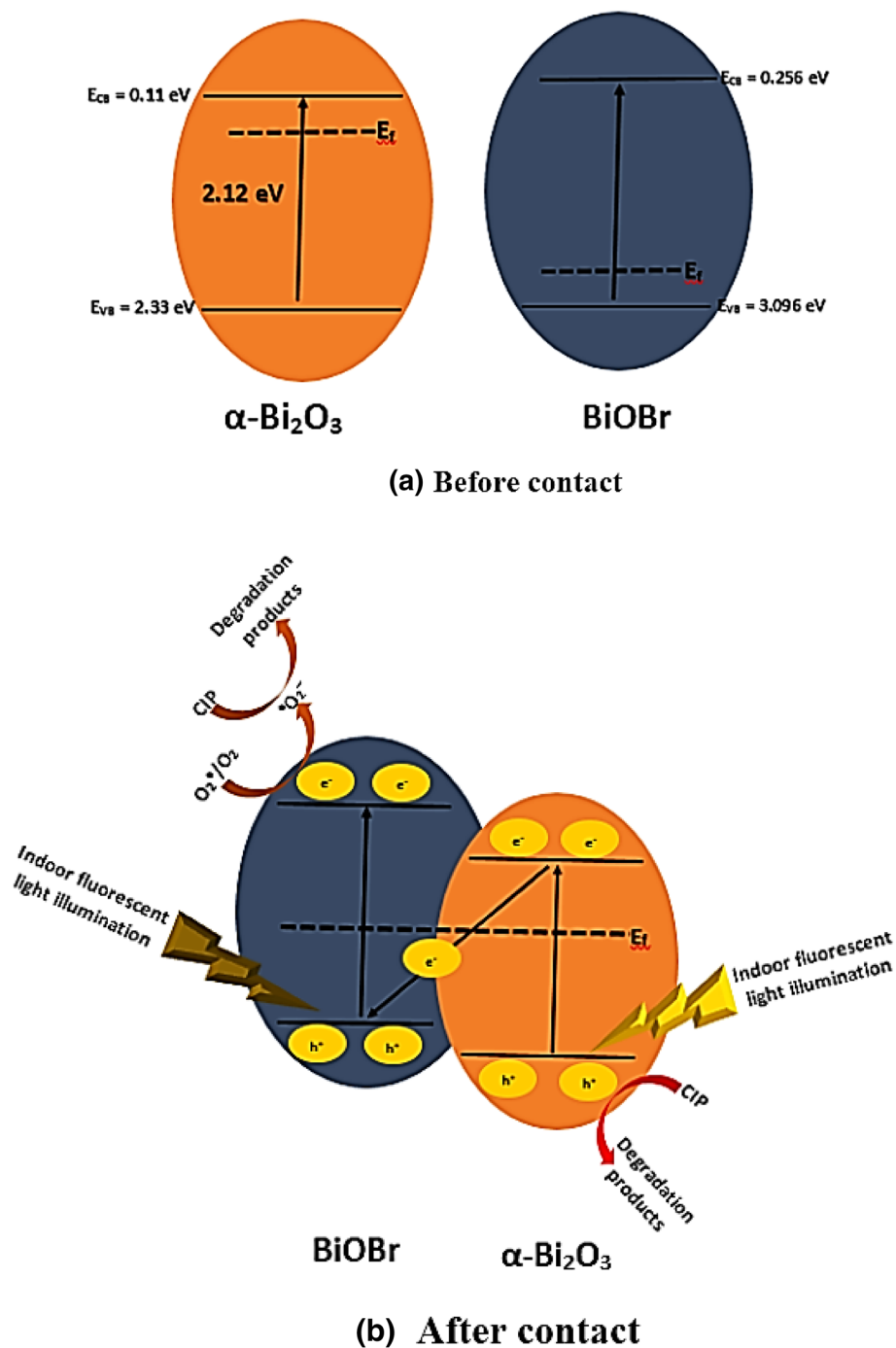


Fig. 13 Photocatalytic degradation (a) and kinetics curve (b) of CIP degradation by BiOBr/Bi₂O₃-60 composite, in the absence and presence of various scavengers, under indoor fluorescent light illumination

Fig. 14 Proposed mechanism for the photocatalytic degradation of CIP over BiOBr/Bi₂O₃-60 composite under indoor fluorescent light illumination



3.12 Reusability studies

The stability of a catalyst in the overall photodegradation process is also an issue of major concern. For such reason, the performance of BiOBr/Bi₂O₃-60 composite photocatalyst towards the degradation of CIP was tested five times. Based on the results presented in Fig. 15, it is clear that, the BiOBr/Bi₂O₃-60 composite photocatalyst maintained a significant performance even after five repeated cycles of

ciprofloxacin degradation. This shows that BiOBr/Bi₂O₃-60 composite photocatalyst is reusable.

4 Conclusion

In summary, BiOBr/Bi₂O₃ composite photocatalysts have been synthesized through a facile room-temperature production process, which combines both technical and

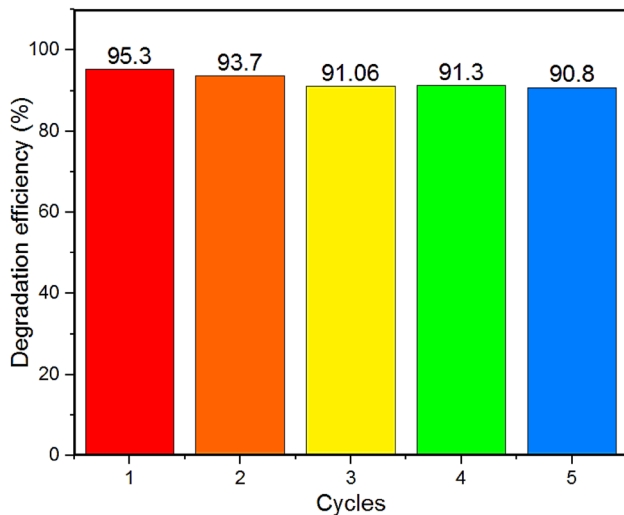


Fig. 15 Reusability studies of BiOBr/Bi₂O₃-60 composite photocatalyst for the degradation of CIP under indoor fluorescent light illumination

economic feasibility. Compared to pristine BiOBr, the BiOBr/Bi₂O₃ composite photocatalysts displayed higher performance for CIP degradation. Among the BiOBr/Bi₂O₃ composite photocatalysts, BiOBr/Bi₂O₃-60 showed the best performance, as it was able to degrade 95.3% of aqueous ciprofloxacin solution (100 mL, 20 ppm) at the rate of 0.02516 min⁻¹ within 90 min. Such enhanced performance is attributed to the formed heterojunction between BiOBr and Bi₂O₃ which improves visible light absorption and inhibits the recombination of photogenerated charge carriers. Furthermore, the BiOBr/Bi₂O₃-60 composite photocatalyst maintained reasonable efficiency even after five cycles, and therefore can be a promising candidate for the treatment of wastewater contaminated by organic pollutants.

Acknowledgements The authors gratefully acknowledge the financial support of Universiti Sains Malaysia through RU Grant No. 304/PKIMIA/6316507.

Compliance with ethical standards

Conflict of interest The authors declare that they have no conflict of interests.

References

- Tang L, Wang J, Zeng G, Liu Y, Deng Y, Zhou Y, Tang J, Wang J, Guo Z (2016) Enhanced photocatalytic degradation of norfloxacin in aqueous Bi₂WO₆ dispersions containing nonionic surfactant under visible light irradiation. *J Hazard Mater* 306:295–304
- Shehu Imam S, Adnan R, Mohd Kaus NH (2018) Photocatalytic degradation of ciprofloxacin in aqueous media: a short review. *Toxicol Environ Chem* 100(5–7):518–539
- Malakootian M, Mahdizadeh H, Dehdarirad A, Amiri Gharaghani M (2018) Photocatalytic ozonation degradation of ciprofloxacin using ZnO nanoparticles immobilized on the surface of stones. *J Dispers Sci Technol* 40:846–854
- Kumar JV, Karthik R, Chen S-M, Muthuraj V, Karuppiah C (2016) Fabrication of potato-like silver molybdate microstructures for photocatalytic degradation of chronic toxicity ciprofloxacin and highly selective electrochemical detection of H₂O₂. *Sci Rep* 6:34149
- Imam SS, Adnan R, Kaus NHM (2018) Influence of yttrium doping on the photocatalytic activity of bismuth oxybromide for ciprofloxacin degradation using indoor fluorescent light illumination. *Res Chem Intermed* 44(9):5357–5376
- Chen M, Chu W (2015) Photocatalytic degradation and decomposition mechanism of fluoroquinolones norfloxacin over bismuth tungstate: experiment and mathematic model. *Appl Catal B* 168:175–182
- Zhang X, Wang Y, Liu B, Sang Y, Liu H (2017) Heterostructures construction on TiO₂ nanobelts: a powerful tool for building high-performance photocatalysts. *Appl Catal B* 202:620–641
- Lam S-M, Sin J-C, Abdullah AZ, Mohamed AR (2013) ZnO nanorods surface-decorated by WO₃ nanoparticles for photocatalytic degradation of endocrine disruptors under a compact fluorescent lamp. *Ceram Int* 39(3):2343–2352
- Bao Y, Lim T-T, Zhong Z, Wang R, Hu X (2017) Acetic acid-assisted fabrication of hierarchical flower-like Bi₂O₃ for photocatalytic degradation of sulfamethoxazole and rhodamine B under solar irradiation. *J Colloid Interface Sci* 505:489–499
- Luo S, Qin F, Zhao H, Liu Y, Chen R (2017) Fabrication uniform hollow Bi₂S₃ nanospheres via Kirkendall effect for photocatalytic reduction of Cr(VI) in electroplating industry wastewater. *J Hazard Mater* 340:253–262
- Wang J, Tang L, Zeng G, Deng Y, Liu Y, Wang L, Zhou Y, Guo Z, Wang J, Zhang C (2017) Atomic scale g-C₃N₄/Bi₂WO₆ 2D/2D heterojunction with enhanced photocatalytic degradation of ibuprofen under visible light irradiation. *Appl Catal B* 209:285–294
- Hu X, Cheng L, Li G (2017) One-pot hydrothermal fabrication of basic bismuth nitrate/BiOBr composite with enhanced photocatalytic activity. *Mater Lett* 203:77–80
- Xue C, Xia J, Wang T, Zhao S, Yang G, Yang B, Dai Y, Yang G (2014) A facile and efficient solvothermal fabrication of three-dimensionally hierarchical BiOBr microspheres with exceptional photocatalytic activity. *Mater Lett* 133:274–277
- Cheng L, Yan J, Zhao S, Hao L (2019) Multiple charge carrier transfer pathways in BiOBr/Bi₂O₃/BiO_{0.67}F_{1.66} ternary composite with high adsorption and photocatalytic performance. *J Alloys Compd* 778:924–932
- Jiang Z, Yang F, Yang G, Kong L, Jones MO, Xiao T, Edwards PP (2010) The hydrothermal synthesis of BiOBr flakes for visible-light-responsive photocatalytic degradation of methyl orange. *J Photochem Photobiol, A* 212(1):8–13
- Gao J, Gao Y, Sui Z, Dong Z, Wang S, Zou D (2018) Hydrothermal synthesis of BiOBr/FeWO₄ composite photocatalysts and their photocatalytic degradation of doxycycline. *J Alloys Compd* 732:43–51
- Cheng L, Hu X, Hao L (2018) Ultrasonic-assisted in situ fabrication of BiOBr modified Bi₂O₃CO₃ microstructure with enhanced photocatalytic performance. *Ultrason Sonochem* 44:137–145
- Han A, Zhang H, Lu D, Sun J, Chuah GK, Jaenicke S (2018) Efficient photodegradation of chlorophenols by BiOBr/NaBiO₃

- heterojunctioned composites under visible light. *J Hazard Mater* 341:83–92
19. Maisang W, Phuruangrat A, Randorn C, Kungwankunakorn S, Thongtem S, Wiranwetchayan O, Wannapop S, Chooopun S, Kaowphong S, Thongtem T (2018) Enhanced photocatalytic performance of visible-light-driven BiOBr/BiPO₄ composites. *Mater Sci Semicond Process* 75:319–326
 20. Sanoop P, Anas S, Ananthakumar S, Gunasekar V, Saravanan R, Ponnusami V (2016) Synthesis of yttrium doped nanocrystalline ZnO and its photocatalytic activity in methylene blue degradation. *Arab J Chem* 9:S1618–S1626
 21. Sundararajan M, Sailaja V, Kennedy LJ, Vijaya JJ (2017) Photocatalytic degradation of rhodamine B under visible light using nanostructured zinc doped cobalt ferrite: kinetics and mechanism. *Ceram Int* 43(1):540–548
 22. Zhang J, Lv J, Dai K, Liang C, Liu Q (2018) One-step growth of nanosheet-assembled BiOCl/BiOBr microspheres for highly efficient visible photocatalytic performance. *Appl Surf Sci* 430:639–646
 23. Cheng L, Kang Y (2014) Synthesis of NaBiO₃/Bi₂O₃ heterojunction-structured photocatalyst and its photocatalytic mechanism. *Mater Lett* 117:94–97
 24. Malathi A, Vasanthakumar V, Arunachalam P, Madhavan J, Ghanem MA (2017) A low cost additive-free facile synthesis of BiFeWO₆/BiVO₄ nanocomposite with enhanced visible-light induced photocatalytic activity. *J Colloid Interface Sci* 506:553–563
 25. Imam SS, Adnan R, Kaus NHM, Hussin MH (2019) Room-temperature synthesis of Bi/BiOBr composites for the catalytic degradation of ciprofloxacin using indoor fluorescent light illumination. *J Mater Sci: Mater Electron* 30(6):6263–6276
 26. Li W, Zou Y, Geng X, Xiao F, An G, Wang D (2017) Constructing highly catalytic oxidation over BiOBr-based hierarchical microspheres: importance of redox potential of doped cations. *Mol Catal* 438:19–29
 27. Lam S-M, Sin J-C, Abdullah AZ, Mohamed AR (2013) Efficient photodegradation of endocrine-disrupting chemicals with Bi₂O₃-ZnO nanorods under a compact fluorescent lamp. *Water Air Soil Pollut* 224(5):1565
 28. Liu Z, Liu J, Wang H, Cao G, Niu J (2016) Boron-doped bismuth oxybromide microspheres with enhanced surface hydroxyl groups: synthesis, characterization and dramatic photocatalytic activity. *J Colloid Interface Sci* 463:324–331
 29. Li Z, Zhang Q, Liu X, Chen M, Wu L, Ai Z (2018) Mechanochemical synthesis of novel heterostructured Bi₂S₃/Zn-Al layered double hydroxide nano-particles as efficient visible light reactive Z-scheme photocatalysts. *Appl Surf Sci* 452:123–133
 30. Hao Z, Xu L, Wei B, Fan L, Liu Y, Zhang M, Gao H (2015) Nanosize α-Bi₂O₃ decorated Bi₂MoO₆ via an alkali etching process for enhanced photocatalytic performance. *RSC Adv* 5(16):12346–12353
 31. Guo Y, Zhang Y, Tian N, Huang H (2016) Homogeneous {001}-BiOBr/Bi heterojunctions: facile controllable synthesis and morphology-dependent photocatalytic activity. *ACS Sustain Chem Eng* 4(7):4003–4012
 32. Zhao C, Li W, Liang Y, Tian Y, Zhang Q (2016) Synthesis of BiOBr/carbon quantum dots microspheres with enhanced photoactivity and photostability under visible light irradiation. *Appl Catal A* 527:127–136
 33. Wang Q, Jiao D, Lian J, Ma Q, Yu J, Huang H, Zhong J, Li J (2015) Preparation of efficient visible-light-driven BiOBr/Bi₂O₃ heterojunction composite with enhanced photocatalytic activities. *J Alloys Compd* 649:474–482
 34. Wu T, Liu L, Pi M, Zhang D, Chen S (2016) Enhanced magnetic and photocatalytic properties of Bi₂Fe₄O₉ semiconductor with large exposed (001) surface. *Appl Surf Sci* 377:253–261
 35. Wang S, Chen Y, Long Y, Li L, Wang L, Zhang S, Jiang F (2018) Room Temperature Synthesis of BiOI/Bi₅O₇ 1-p-n Heterojunction with Enhanced Photocatalytic Activity for 17α-Ethinylestradiol. *Chem Sel* 3(28):8095–8105
 36. Ye Z, Xiao X, Chen J, Wang Y (2019) Fabrication of BiVO₄/BiOBr composite with enhanced photocatalytic activity by a CTAB-assisted polyol method. *J Photochem Photobiol, A* 368:153–161
 37. Yu C, Zhou W, Zhu L, Li G, Yang K, Jin R (2016) Integrating plasmonic Au nanorods with dendritic like α-Bi₂O₃/Bi₂O₂CO₃ heterostructures for superior visible-light-driven photocatalysis. *Appl Catal B* 184:1–11
 38. Yang K, Li J, Peng Y, Lin J (2017) Enhanced visible light photocatalysis over Pt-loaded Bi₂O₃: an insight into its photogenerated charge separation, transfer and capture. *Phys Chem Chem Phys* 19(1):251–257
 39. Xa Dong, Zhang W, Sun Y, Li J, Cen W, Cui Z, Huang H, Dong F (2018) Visible-light-induced charge transfer pathway and photocatalysis mechanism on Bi semimetal@ defective BiOBr hierarchical microspheres. *J Catal* 357:41–50
 40. Guo J-g, Liu Y, Hao Y-j, Li Y-l, Wang X-j, Liu R-h, Li F-t (2018) Comparison of importance between separation efficiency and valence band position: the case of heterostructured Bi₃O₄Br/α-Bi₂O₃ photocatalysts. *Appl Catal B* 224:841–853

Publisher's Note Springer Nature remains neutral with regard to jurisdictional claims in published maps and institutional affiliations.